

Operando visualisation of kinetically-induced lithium heterogeneities in single-particle layered Ni-rich cathodes

Chao Xu^{1,2,3,4†}, Alice J. Merryweather^{1,2,3†}, Shrinidhi S. Pandurangi^{3,5}, Zhengyan Lun^{1,2,3}, David S. Hall^{1,3}, Vikram S. Deshpande^{3,5}, Norman A. Fleck^{3,5}, Christoph Schnedermann^{2,3*}, Akshay Rao^{2,3*}, Clare P. Grey^{1,3*}

¹Yusuf Hamied Department of Chemistry, University of Cambridge; Cambridge, UK

²Cavendish Laboratory, University of Cambridge; Cambridge, UK

³The Faraday Institution; Quad One, Harwell Science and Innovation Campus, Didcot, UK

⁴School of Physical Science and Technology, ShanghaiTech University; Shanghai, China

⁵Department of Engineering, University of Cambridge; Cambridge, UK

*Corresponding author. Email: cs2002@cam.ac.uk (C.S.); ar525@cam.ac.uk (A.R.); cpg27@cam.ac.uk (C.P.G)

†These authors contributed equally to this work

Abstract: Understanding how lithium-ion dynamics affect the (de)lithiation mechanisms of state-of-the-art nickel-rich layered oxide cathodes is crucial to improving electrochemical performance. Here, we directly observe two distinct kinetically-induced lithium heterogeneities within single-crystal $\text{LiNi}_x\text{Mn}_y\text{Co}_{(1-x-y)}\text{O}_2$ (NMC) particles using recently developed *operando* optical microscopy, challenging the notion that uniform (de)lithiation occurs within individual particles. Upon delithiation, a rapid increase in lithium diffusivity at the beginning of charge results in particles with lithium-poor peripheries and lithium-rich cores. The slow ion diffusion at near-full lithiation states – and slow charge transfer kinetics – also leads to heterogeneity at the end of discharge, with a lithium-rich surface preventing complete lithiation. Finite-element modelling confirms that concentration-dependent diffusivity is necessary to reproduce these phenomena. Our results show that diffusion limitations cause first-cycle capacity losses in Ni-rich cathodes.

Layered Ni-rich NMCs ($\text{LiNi}_x\text{Mn}_y\text{Co}_{(1-x-y)}\text{O}_2$, $x \geq 0.5$) and NCAs ($\text{LiNi}_x\text{Co}_y\text{Al}_{(1-x-y)}\text{O}_2$, $x \geq 0.5$) are widely used as cathode materials in high energy density lithium-ion batteries for electric vehicle applications (1–4). Despite their cost and environmental benefits, these cathode materials suffer from long-term stability issues that limit their safety and lifetime, as well as typical irreversible capacity losses of >10% during the first cycle (5–7). Significant world-wide effort is thus being devoted to understanding their underlying charging mechanisms to mitigate these shortcomings (3, 8, 9). Previous studies have attributed the first-cycle capacity losses to kinetic limitations due to slow lithium diffusion at near-full lithiation states, as a result of fewer lithium vacancies and decreased interlayer spacing (10, 11). X-ray diffraction (XRD)-based methods have furthermore revealed several “phase segregation” phenomena during the delithiation of Ni-based layered cathodes (12–15), despite the fact that the (de)lithiation of such materials intrinsically follows a solid-solution mechanism (12, 16, 17). Rather than a thermodynamic phase segregation, these observations suggest formation of kinetically-controlled heterogeneities in lithium occupancy that occur over a sufficient domain size or length-scale to result in discernible differences in the lattice constants and diffraction signals; however, a debate exists as to whether this heterogeneity is at the particle or electrode level (14).

These proposed lithium heterogeneity phenomena are closely correlated with the electrochemical performance of the cathode material. However, our understanding of the operative mechanism by which the heterogeneity arises at the particle level is limited, since many of these studies are based on ensemble characterisation techniques, particularly *in-situ* and *ex-situ* X-ray diffraction of bulk electrodes, where the measurements inherently cannot spatially resolve the heterogeneity at the relevant length-scales (12, 13). Recent advances in synchrotron-based micro-spectroscopy techniques, such as scanning transmission X-ray microscopy (STXM) coupled with X-ray absorption spectroscopy (14, 18–20), are capable of providing chemical information at the nanometre scale. However, such techniques suffer from disadvantages including limited availability to beam time and potential beam damage (21).

In this work, we directly track the lithium-ion dynamics in monolithic (also referred to as “single-crystal”) Ni-rich NMC cathodes, with a particular focus on the transient lithium heterogeneities during lithium insertion and extraction, using a recently developed method – *operando* optical scattering microscopy (22). Our results demonstrate a clear correlation between the optical intensity and local lithium content, and we identify kinetically-induced lithium heterogeneities within individual active NMC particles. These heterogeneities are most prominent at the beginning of charge and also appear at the end of discharge, originating from a sharp drop in the lithium-ion diffusion coefficient toward high lithium contents. We further explore the origins of these phenomena with finite-element modelling parameterised by a lithium concentration-dependent diffusion coefficient, derived from electrochemical characterisation. This combined approach enables us to determine the effects of the rate-limiting kinetic processes on the (de)lithiation of Ni-rich NMC cathodes and identify the conditions under which lithium heterogeneity occurs at the individual particle level. Via experiment and theory we determine the origin of the first cycle capacity loss in NMCs.

***Operando* optical scattering microscopy**

During a typical *operando* measurement, an optically-accessible electrochemical cell (Fig. 1A) operates either under a constant-current or a constant-voltage bias, and is simultaneously illuminated with a light-emitting diode (LED, central wavelength of 740 nm). The reflected and back-scattered light from the sample and the glass/electrolyte interface are collected and imaged onto a camera. Fig. 1B shows an optical image of part of the NMC cathode with nominal

stoichiometry $\text{LiNi}_{0.88}\text{Mn}_{0.05}\text{Co}_{0.07}\text{O}_2$, where the bright area corresponds to an individual $\sim 2 \mu\text{m}$ NMC particle and the surrounding dark area represents the conductive carbon and binder matrix. The observed optical intensity is partly determined by the local dielectric properties of the particle (23–25), which are sensitive to the degree of lithiation.

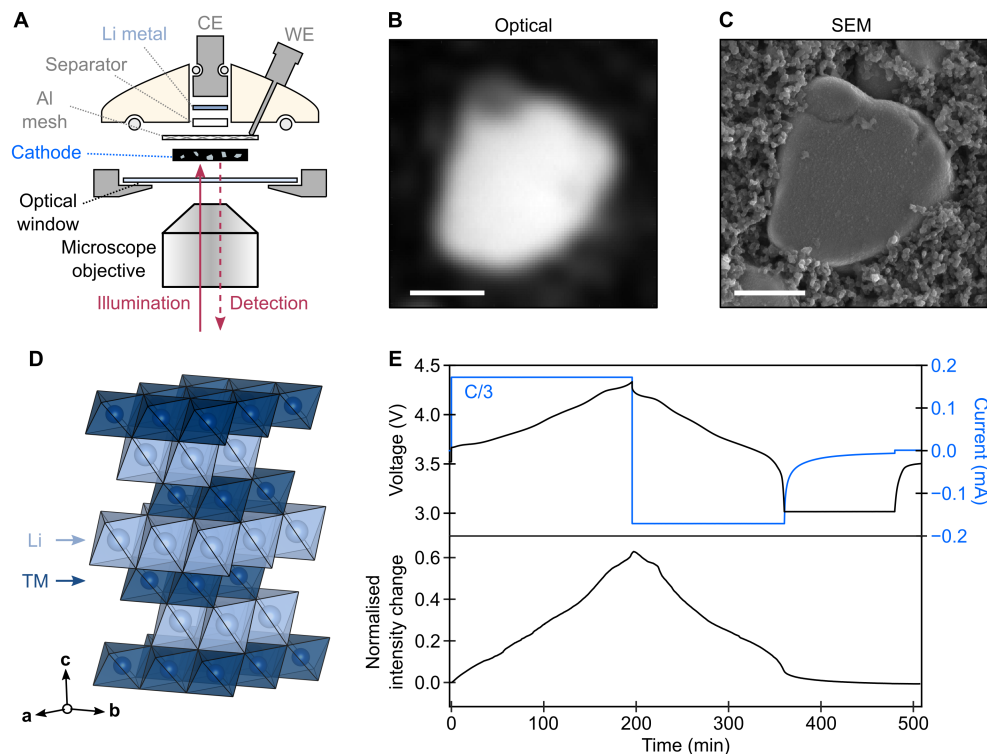


Fig. 1. Monolithic NMC cathode and operando optical microscopy. (A) Schematic drawing of the key components of the electrochemical cell for optical microscopy. The cathode is a self-standing electrode composed of numerous NMC particles, carbon black and polytetrafluoroethylene (PTFE) binder. Aluminium mesh is used as a current collector. (WE = working electrode, CE = counter electrode). (B) Optical image of an active NMC particle in the electrochemical cell. (C) SEM image of the same monolithic NMC particle shown in (B), obtained after the optical measurements. (D) Schematic illustration of the crystal structure of the NMC cathode illustrating the alternating layers of LiO_6 and TMO_6 octahedra, where TM denotes transition metal. (E) Voltage (black) and current (blue) profile (top panel) and the normalised optical intensity of the active particle shown in (B) (bottom panel) during one charge-discharge cycle (comprising a C/3 constant-current (CC) charge and discharge between 4.3 and 3 V, followed by a two-hour constant-voltage (CV) hold at 3 V). Three C/3 cycles were performed prior to this cycle, finishing with two-hour voltage holds at 3 V. The C-rate was calculated based on a practical capacity of 210 mA h g^{-1} , i.e., the current density for C/3 rate is 70 mA g^{-1} . Scale bars, $1 \mu\text{m}$.

The uniform optical intensity across the particle suggests that the top surface is smooth and flat, as further confirmed by a scanning electron microscope (SEM) image of the same particle (Fig. 1C). Moreover, the flat surface is a strong indication that the observed surface is parallel to the NMC a/b basal plane (see the structure illustration in Fig. 1D).

X-ray diffraction confirms the NMC is phase pure (space group $R\bar{3}m$) and has a low Li/Ni antisite mixing ($\sim 2\%$; diffraction pattern and Rietveld refinement results shown in fig. S1). Fig. 1E shows a typical voltage (black line) and current (blue line) profile for a constant-current (CC) charge – constant-current constant-voltage (CCCV) discharge cycle at $C/3$ rate (nC corresponds to a full charge or discharge in $1/n$ hours), with a two-hour voltage hold at 3 V at the end of discharge (full electrochemical cycling history is summarised in fig. S2). The CC charge and CC discharge capacities were $229.0 \text{ mA h g}^{-1}$ and $192.4 \text{ mA h g}^{-1}$, respectively, corresponding to a coulombic efficiency of 84.0%. The two-hour hold at 3 V provided an additional 16.4 mA h g^{-1} , increasing the coulombic efficiency to 91.2%. The extra discharge capacity obtained by applying a constant voltage (CV) step at the end of CC discharge is a generic behaviour for all layered Ni-rich cathodes (5, 13). Note that even with a CV hold, the coulombic efficiency of 91.2% is lower than that achieved in coin cells with an equivalent electrode and cycling procedure (typically $>99\%$ after the first cycle; see fig. S3), which we attribute to the performance limitations of the specialised *operando* cell.

On charge, the optical intensity of the active particle increases monotonically as lithium is de-intercalated from the NMC particle, reaching a maximum intensity $\sim 62\%$ higher than its initial value; the general trend is reversed on discharge/lithiation (bottom panel in Fig. 1E; movie S1). This clearly shows that the dielectric properties of the NMC cathode are strongly dependent on its lithium content. Moreover, the monotonic nature of the intensity change means that intensity can be used as a qualitative proxy for the single-particle state-of-charge (SoC)/lithium content: a higher intensity corresponds to a lower lithium content. A more detailed analysis of the relationship between the optical intensity and lithium content is given in fig. S4 and the smaller changes seen above 4.1 V are shown in fig. S5.

Lithium heterogeneity at the beginning of charge

We now investigate spatially-resolved delithiation and lithiation processes in single-particle NMCs. Fig. 2A shows the voltage profile and intensity change during the first hour of the $C/3$ charge, and differential images (see Methods) with respect to the beginning of the cycle at 5, 15, 25 and 35 min are shown in Fig. 2B. After 5 min of delithiation at $C/3$, the periphery of the particle started to show a positive contrast, the higher intensity being ascribed to local NMC domains with lower lithium content (higher intensity is indicative of lower lithium content; Fig. 1D). The core remains fully lithiated and a distinct lithium concentration heterogeneity inside this individual NMC particle is formed. On further charging, this periphery continued to advance towards the centre of the particle, further increasing in positive contrast, while the core lagged noticeably behind (15 and 25 min, Fig. 2B). After 35 min, the total contrast had become reasonably uniform across the whole particle (movie S2). We have observed this phenomenon in more than 50 different particles from seven different electrodes, confirming its reproducibility (see fig. S6).

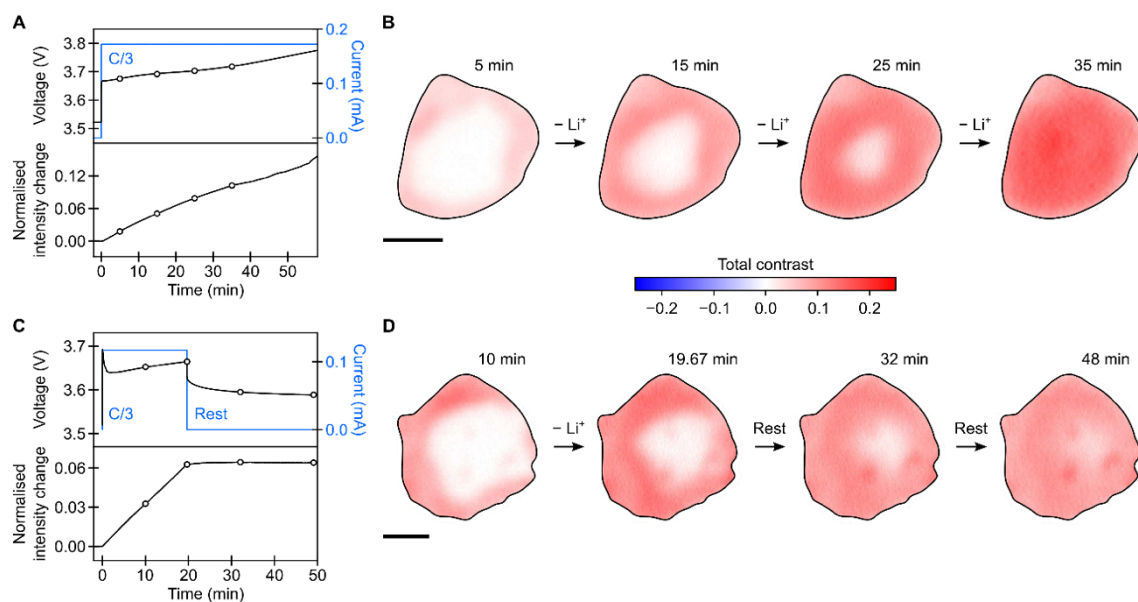


Fig. 2. Lithium heterogeneity in single-particle NMC at the beginning of charge. (A) Voltage and current profiles during the first one hour of charge at C/3 (top panel), and the normalised intensity changes, obtained by integrating over the whole active particle shown in (B) (bottom panel). (B) Normalised differential images of the active particle during the initial charging, for the time points indicated by black circles in (A). The total contrast is shown, which represents the fractional intensity change between the current frame and the first frame of the cycle (i.e., with no current applied). The colour scale is centred at zero (white), with positive values indicating an overall intensity increase (red) and negative values indicating a decrease (blue). (C) Voltage and current profiles during the first 20 min of charge at C/3 followed by a rest period (top panel), and the normalised intensity changes of the active particle (bottom panel). (D) Normalised differential images of the active NMC particle during the charge-rest experiment. Scale bars, 1 μm .

This apparent “core-shell” structure cannot be of thermodynamic origin, since (de)lithiation of Ni-rich materials is widely acknowledged to be a solid-solution process. This is in contrast to the closely related material LiCoO_2 , which exhibits a thermodynamic two-phase region at the beginning of charge caused by an insulator-to-metal transition, absent in NMC (26–28). A charge-rest experiment was then performed to confirm the kinetic origin of the “core-shell” structure observed here (Fig. 2C). During the ~ 20 -minute charge period, lithium heterogeneity began to develop in the particle as described above (Fig. 2D). After stopping the current, however, the intensity heterogeneity across the particle gradually disappeared, and a uniform distribution was achieved by the end of the rest period (Fig. 2D); this is consistent with a kinetically-driven intra-particle heterogeneity where the equilibrium state exhibits a uniform lithium distribution.

In addition to the intra-particle heterogeneity discussed above, some inter-particle reaction heterogeneity was also observed at the beginning of charge at a higher rate of 2C (fig. S7). We ascribe this observation to differences in wiring and tortuosity of pathways for lithium transport through the bulk electrode to the NMC particles (movie S3). Further studies are currently underway to quantify these effects.

Finite-element modelling and rate dependence

Guided by the experimental results, we developed a finite-element model to assist our understanding of the lithium heterogeneity observed at the beginning of charge. Our modelling assumes a constant lithium flux in/out of a particle with the same cross-sectional shape as that examined experimentally (Fig. 3A), with diffusion restricted to within the basal plane of the particle. To parameterise the model, we measured the lithium chemical diffusion coefficient, D_{Li} , using galvanostatic intermittent titration experiments (GITT) as a function of SoC. However, the absolute value of D_{Li} depends strongly on assumptions made as part of the analysis, including the distance L that the lithium-ions travel during the relaxation time of the GITT experiment, which may vary as a function of particle size and shape (29, 30), defects in the particle (31, 32), orientation of particles within the electrode, and even the tortuosity of the path taken by the ions within the electrode to reach the active materials (33).

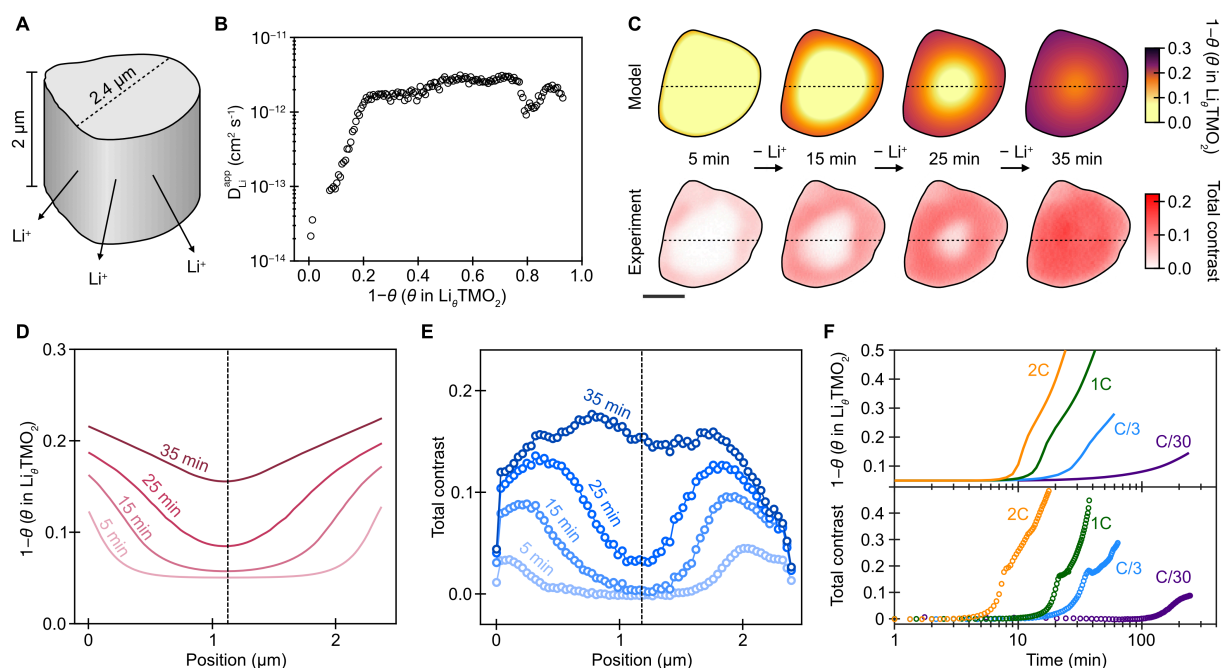


Fig. 3. Comparing modelling and experiments. (A) Schematic illustration of the particle used in the modelling. (B) The apparent lithium diffusion coefficient $D_{\text{Li}}^{\text{app}} \equiv \alpha D_{\text{Li}}$ as a function of lithium content ($\alpha = 2.7$). (C) Comparison of simulation and experimental imaging results, both conducted at a delithiation rate of $C/3$. The modelling results show the degree of delithiation ($1 - \theta$) on the basal plane of the particle at various times during the charge. (D, E) Evolution of (D) the degree of delithiation in the simulation and (E) the total contrast in the optical images along the horizontal dashed line marked in (C). (F) Evolution of the degree of delithiation (simulation, top panel) and total contrast (optical images, bottom panel) at the centre of the particle (shown by the vertical dashed lines in (D) and (E)).

Instead of relying on its absolute value, we scaled the GITT-retrieved chemical diffusion coefficient, D_{Li} , by a constant factor to generate $D_{\text{Li}}^{\text{app}}$ ($D_{\text{Li}}^{\text{app}} \equiv \alpha D_{\text{Li}}$), which we then compared to the optical results at a charging rate of $C/3$. We found the best match to the experiment for values close to $\alpha = 2.7$. This scaling factor gives rise to $D_{\text{Li}}^{\text{app}} \sim 10^{-14} \text{ cm}^2 \text{ s}^{-1}$ near full lithiation, which

increases by almost two orders of magnitude upon removal of 20% of the lithium (Fig. 3B). As shown in Figs. 3C-E, our model clearly captured the experimentally-observed development of pronounced lithium concentration gradients within the particle during delithiation at a charging rate of $C/3$. This lithium heterogeneity was also well reproduced by our experiments and model for charging rates from $C/30$ to $2C$ (figs. S8-11). Importantly, the general feature of heterogeneous delithiation with a lithium poor periphery is independent of the scaling factor over a range of $1 \leq \alpha \leq 5$ for the particle in Fig. 3A. For larger values of α , diffusion becomes sufficiently rapid that the particle delithiates approximately uniformly (fig. S12).

The lithium heterogeneity during charging can be succinctly illustrated by retrieving the lithium content at the centre of the particle (Fig. 3F). Again, the model is in good agreement with experimental results and clearly shows that the delithiation of the particle centre lags noticeably behind the start of the CC charge at all charging rates, indicating that the delithiation front takes significant time to reach the centre. Our model also indicates that the intra-particle heterogeneity is strongly dependent on the particle size, i.e., smaller particles show less pronounced heterogeneity (figs. S13, S14). We note that our modelling revealed that some spatial lithium-ion heterogeneity can also arise in the case of a low constant-value of the ion diffusivity ($D_{Li} < 10^{-13} \text{ cm}^2 \text{ s}^{-1}$, fig. S13). However, for these constant diffusivities, the ion concentration in the centre of the particle increases linearly over time (fig. S15), in contrast to the experimentally-observed non-linear trend (Fig. 3F). Taken together, these results strongly support our hypothesis that the observed heterogeneous delithiation is a result of the steep change in diffusivity with changing lithium content at the beginning of charge.

Lithium heterogeneity at the end of discharge

We next explored in more detail how these dynamic lithium heterogeneities influence the first cycle capacity loss in layered Ni-rich materials. During CC cycling at $1C$ (Fig. 4A), the normalised intensity of the particle followed the same trends as seen above. Importantly, however, at the end of discharge, the particle intensity was 8% higher than its initial value, indicating incomplete reinsertion of lithium, in line with the voltage-capacity profile (fig. S2). During a subsequent two-hour CV hold at 3 V, an extra capacity of $\sim 24 \text{ mA h g}^{-1}$ could be extracted (increasing the coulombic efficiency from 82.3% to 94.3%) and the mean intensity reached its initial value.

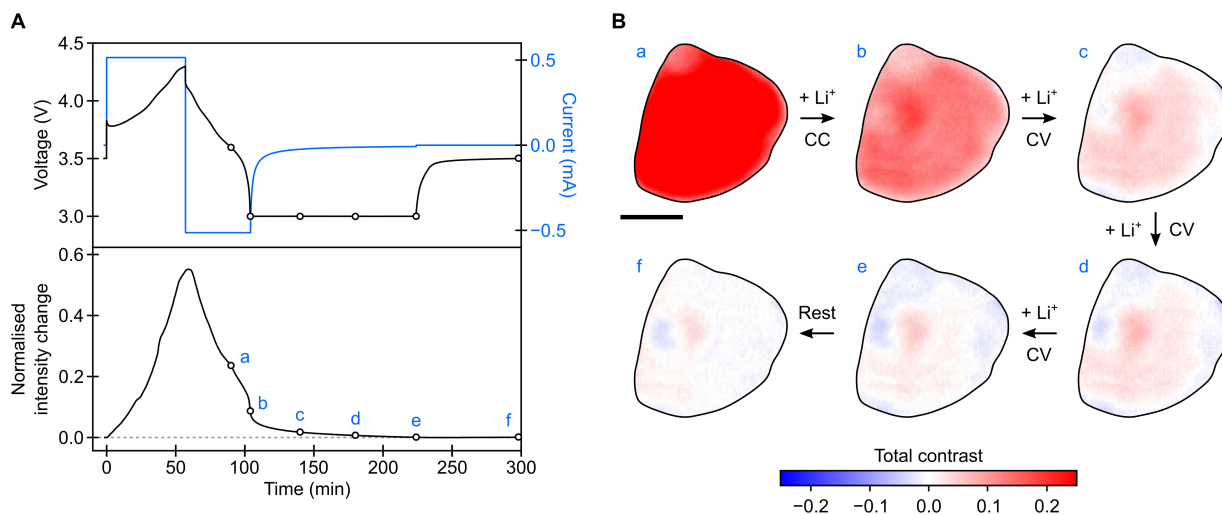


Fig. 4. Lithium heterogeneity at the end of discharge. (A) Voltage and current profile (top panel) and normalised intensity changes of the active particle during a 1C rate CC charge and CCCV discharge cycle. CV was performed at 3 V for two hours. The dashed grey line (bottom panel) is a guide for the eye, representing 0 intensity change. The initial lithium content is estimated to be ~97% based on the open circuit voltage (OCV, ~3.5 V vs. Li/Li⁺). Note this near-full lithiation state was achieved by applying a two-hour voltage hold at 3 V after the end of CC discharge in the previous cycle. (B) Differential images of an NMC active particle during the discharge, at the times indicated by black circles in (A) (where a, b, c, d, e and f are at 90, 104, 140, 180, 224 and 298 min, respectively). Scale bars, 1 μm . The current at the end of the CV period was $-7.59 \mu\text{A}$ (equivalent to $\sim C/200$; negative sign denotes discharging current).

Examining the spatial intensity variations across the particle shows that the intensity of the active particle remained uniform for the first 30 min of the 1C discharge (a in Fig. 4B). At the end of the CC discharge (104 min, b in Fig. 4B), the vast majority of the particle still exhibited a lower lithium content (positive total contrast – red) compared to the beginning of charge. Yet, around a narrow periphery of the particle the total contrast was close to zero (fig. S16), indicating that the particle has a lithium-rich periphery (with the lithium content approaching that of the particle before charging) and a more lithium-deficient core.

The fact that the core remains lithium deficient can be explained by the drastically reduced lithium diffusion coefficient and charge transfer kinetics (11, 14) at near-full lithiation states (fig. S18). Both of these two kinetic limitation factors can lead to high over-potentials and result in the steep decrease in the voltage that quickly reaches the cut-off value (3 V in the present case). Furthermore, the non-uniform lithium distribution also indicates that the lithium insertion is primarily diffusion-limited. Such lithium heterogeneities near the end of discharge are also seen in our modelling: for an occupancy of $(1 - \theta) < 0.2$, the drop in diffusivity produces a significant concentration gradient across the particle, which is more pronounced with faster charging rates (fig. S17).

With the additional CV step, the particle was re-lithiated further as indicated by the continued decrease in total contrast (c, d, e in Fig. 4B). In particular, a large fraction of the particle returned to the initial intensity (~ 0 total contrast, white), confirming that the capacity loss induced by the kinetic limitations mentioned above can be, to a large extent, recovered by a slow lithiation step. At the end of the CV step (e in Fig. 4B), the variation in the contrast (hence the lithium content) across the particle becomes very small, and further equilibration is seen after the open circuit voltage (OCV) rest (f in Fig. 4B).

Discussion

Lithium heterogeneities during delithiation and lithiation (summarised in Fig. 5). When delithiating the layered cathodes from full (and near-full) lithiation states, a noticeable lithium heterogeneity is seen with a lithium-rich core and a lithium-poor periphery. The SoC range during which this heterogeneity is present is dependent on the initial state of charge as well as the charging rate. This lithium heterogeneity arises from the low lithium diffusivity at near-full lithiation, which is insufficient to support a high lithium-ion flux uniformly throughout the particle. Instead, as the lithium is extracted from the periphery of the particle, the periphery develops a higher lithium diffusivity due to its lower lithium occupancy, accelerating the rate of lithium-ion extraction from the lithium-poor periphery domains further. Simultaneously, the boundary between the lithium-

rich and lithium-poor domains propagates towards the centre of the particle as the charging progresses, until the particle becomes uniform in lithium content, and no obvious heterogeneity occurs during the rest of charging.

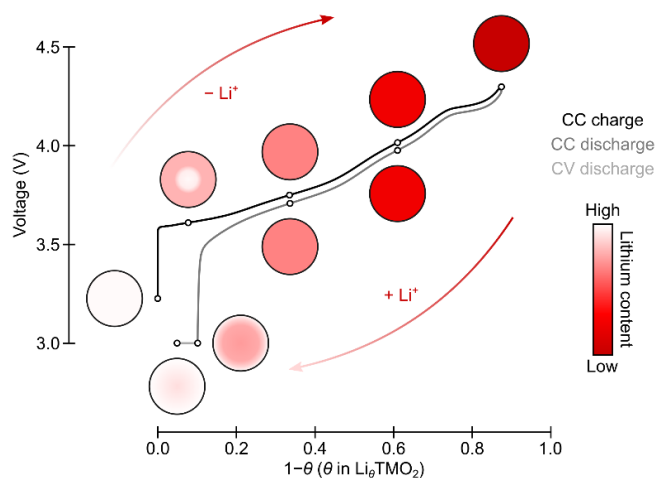


Fig. 5. Summary of the lithium-ion distribution within the single active particle at various lithium contents. The circles show schematic representations of single-particle Ni-rich materials at various SoCs. The voltage profile is illustrative of the single-crystal NMC material used in this work, and was obtained in a half-cell cycled with a CC charge and CC discharge (C/20 rate) and a discharge CV hold at 3 V (for 24 hours).

During CV discharge, lithium insertion occurs predominantly uniformly throughout the particle, except at the very end where a narrow periphery becomes notably lithium-rich compared to the core. This results from two kinetic limitations, slow lithium diffusion – seen by GITT measurements – and slow charge transfer kinetics (see potentiostatic intermittent titration results in fig. S18), both of which lead to a substantial increase in the over-potential, and hence a steep decrease in the cell voltage during CC discharge. As a result, the cell quickly reaches the cut-off voltage with the core of the NMC particles in a lithium-deficient state and therefore causing a capacity loss. Such kinetic limitations can be largely overcome by a much slower lithiation process, for instance, by inserting a CV hold at 3 V vs. Li/Li^+ in the present case. While the degree of heterogeneity at the end of discharge is much less significant than that seen at the beginning of charge, it is nonetheless capable of resulting in a loss in capacity of as much as 10% when using standard CC cycling regimes.

Lithium heterogeneity in related NCA materials at the beginning of the first charge was proposed recently by Grenier et al. (13), in the SoC range of $0.96 > \theta > 0.74$ on the basis of *operando* synchrotron powder XRD. Here, the XRD pattern was modelled with two different phases, with the difference in lithium content between the lithium-poor and the lithium-rich phase gradually increasing from 0.09 at $\theta = 0.96$ to 0.18 at $\theta = 0.74$; such lithium heterogeneity was ascribed to be intra-particle. XRD, however, is a bulk technique and provides no spatially-resolved information. Conversely, Park et al. (14) recently suggested, on the basis of *ex-situ* X-ray absorption microscopy experiments that this heterogeneity occurs between, rather than within, particles. They proposed an intrinsic mechanism for the apparent phase separation observed during the delithiation of NMC,

termed “electro-autocatalysis”, which describes the increase in the interfacial exchange current as lithium content decreases (14).

Our work expands on these studies, directly demonstrating that both proposed mechanisms will be at play under operating conditions. Critically, the intra-particle heterogeneity observed in our work cannot be captured by *ex-situ* experiments (see Fig. 2D). We further note that non-uniform lithiation during the CC and CV discharge has not been previously seen by XRD (13), presumably because it represented a very small fraction of the bulk, highlighting the unique capability of our optical imaging technique to capture the transient and small heterogeneities in battery materials.

Practical implications. The lithium heterogeneity at the beginning of charge will generate a noticeable difference in lattice constants between the lithium-rich and lithium-poor domains. At fast C-rates, for instance, 1C and 2C, the SoC difference between the periphery and the core can be as large as 20-30% within a narrow length-scale based on our modelling (fig. S11). This large concentration gradient will lead to internal stress/strain within individual particles which may further result in mechanical degradation such as particle fracturing, especially for larger particle sizes. Moreover, the first cycle coulombic efficiency loss is of particular importance since it reduces the energy density of practical cells: while graphite anode performances have been continuously improved with the first cycle coulombic efficiencies now approaching 96% (34), that of the Ni-rich materials is limited to ~90%. Therefore, increasing the first-cycle efficiency of the cathode can lead to a direct increase in the reversible energy density at the cell level. Such an increase will be more evident for the next-generation of high energy-density batteries consisting of a Ni-rich cathode and a lithium metal anode. Our results show that the key to improving performance lies in increasing the lithium mobility and charge transfer kinetics at near-full lithiation states. While current literature is yet inconclusive as to what may be the most effective approaches to improve the first cycle coulombic efficiency, certain coating materials – for instance, Nb-containing compounds (35) – have been shown to be promising.

Conclusion remarks

In this work, we employed *operando* optical microscopy to track the lithium-ion dynamics in single-particle layered Ni-rich NMC, with a particular focus on understanding the transient lithium heterogeneities at the single-particle scale. The observed optical intensity revealed a substantial increase upon delithiation (charge) and decrease upon lithiation (discharge), indicating that the optical intensity can be used as a qualitative probe for the local lithium content.

The spatially resolved intensity changes showed clear lithium heterogeneity at the beginning of charge, exhibiting particles with a lithium-poor periphery and lithium-rich core. This intra-particle heterogeneity persisted across a wide range of C-rates, from C/30 to 2C. By developing a finite-element model, we demonstrated that this phenomenon is due to a kinetic diffusion-driven mechanism, caused by low lithium diffusivity at near-full lithiation states which increases dramatically on delithiation. Combining the optical results with electrochemical diffusion measurements and modelling, we extracted accurate values for the concentration-dependent lithium-ion diffusion coefficient of the Ni-rich NMC cathode material under study.

We further showed that when approaching high lithiation states on discharge, the NMC particle surface gradually becomes saturated by lithium, due to the decreased lithium diffusivity at high lithiation states. Coupled with slow charge transfer kinetics, this is the main reason for the first-cycle coulombic inefficiency of layered Ni-rich materials. These results pave the way toward a better understanding of possible improvements in current state-of-the-art NMC materials, and

more broadly highlight the importance of understanding nanoscale dynamic changes in battery materials during their operation.

References and Notes

1. G. E. Blomgren, The Development and Future of Lithium Ion Batteries. *J. Electrochem. Soc.* **164**, A5019 (2016). doi:10.1149/2.0251701jes
2. W. Li, E. M. Erickson, A. Manthiram, High-nickel layered oxide cathodes for lithium-based automotive batteries. *Nat. Energy* **5**, 26 (2020). doi:10.1038/s41560-019-0513-0
3. J. U. Choi, N. Voronina, Y.-K. Sun, S.-T. Myung, Recent Progress and Perspective of Advanced High-Energy Co-Less Ni-Rich Cathodes for Li-Ion Batteries: Yesterday, Today, and Tomorrow. *Adv. Energy Mater.* **10**, 2002027 (2020). doi:10.1002/aenm.202002027
4. C. P. Grey, D. S. Hall, Prospects for lithium-ion batteries and beyond—a 2030 vision. *Nat. Commun.* **11**, 6279 (2020). doi:10.1038/s41467-020-19991-4
5. H. Zhou, F. Xin, B. Pei, M. S. Whittingham, What Limits the Capacity of Layered Oxide Cathodes in Lithium Batteries. *ACS Energy Letters* **4**, 1902 (2019). doi:10.1021/acseenergylett.9b01236
6. Q. Xie, W. Li, A. Manthiram, A Mg-Doped High-Nickel Layered Oxide Cathode Enabling Safer, High-Energy-Density Li-Ion Batteries. *Chem. Mater.* **31**, 938 (2019). doi:10.1021/acs.chemmater.8b03900
7. U.-H. Kim, G.-T. Park, B.-K. Son, G. W. Nam, J. Liu, L.-Y. Kuo, P. Kaghazchi, C. S. Yoon, Y.-K. Sun, Heuristic solution for achieving long-term cycle stability for Ni-rich layered cathodes at full depth of discharge. *Nat. Energy* **5**, 860 (2020). doi:10.1038/s41560-020-00693-6
8. W. Li, X. Liu, H. Celio, P. Smith, A. Dolocan, M. Chi, A. Manthiram, Mn versus Al in Layered Oxide Cathodes in Lithium-Ion Batteries: A Comprehensive Evaluation on Long-Term Cyclability. *Adv. Energy Mater.* **8**, 1703154 (2018). doi:10.1002/aenm.201703154
9. H.-H. Ryu, B. Namkoong, J.-H. Kim, I. Belharouak, C. S. Yoon, Y.-K. Sun, Capacity Fading Mechanisms in Ni-Rich Single-Crystal NCM Cathodes. *ACS Energy Lett.* 2726 (2021). doi:10.1021/acseenergylett.1c01089
10. K. Märker, C. Xu, C. P. Grey, Operando NMR of NMC811/Graphite Lithium-Ion Batteries: Structure, Dynamics, and Lithium Metal Deposition. *J. Am. Chem. Soc.* **142**, 17447 (2020). doi:10.1021/jacs.0c06727
11. M. Ge, S. Wi, X. Liu, J. Bai, S. Ehrlich, D. Lu, W. Lee, Z. Chen, F. Wang, Kinetic Limitations in Single-Crystal High-Nickel Cathodes. *Angew. Chem. Int. Ed.* **60**, 17350 (2021). doi:10.1002/anie.202012773
12. A. Grenier, H. Liu, K. M. Wiaderek, Z. W. Lebens-Higgins, O. J. Borkiewicz, L. F. J. Piper, P. J. Chupas, K. W. Chapman, Reaction Heterogeneity in $\text{LiNi}_{0.8}\text{Co}_{0.15}\text{Al}_{0.05}\text{O}_2$ Induced by Surface Layer. *Chem. Mater.* **29**, 7345 (2017). doi:10.1021/acs.chemmater.7b02236
13. A. Grenier, P. J. Reeves, H. Liu, I. D. Seymour, K. Märker, K. M. Wiaderek, P. J. Chupas, C. P. Grey, K. W. Chapman, Intrinsic Kinetic Limitations in Substituted Lithium-Layered

- Transition-Metal Oxide Electrodes. *J. Am. Chem. Soc.* **142**, 7001 (2020). doi:10.1021/jacs.9b13551
14. J. Park, H. Zhao, S. D. Kang, K. Lim, C. C. Chen, Y. S. Yu, R. D. Braatz, D. A. Shapiro, J. Hong, M. F. Toney, M. Z. Bazant, W. C. Chueh, Fictitious phase separation in Li layered oxides driven by electro-autocatalysis. *Nat. Mater.* **20**, 991 (2021). doi:10.1038/s41563-021-00936-1
 15. C. Xu, K. Märker, J. Lee, A. Mahadevegowda, P. J. Reeves, S. J. Day, M. F. Groh, S. P. Emge, C. Ducati, B. Layla Mehdi, C. C. Tang, C. P. Grey, Bulk fatigue induced by surface reconstruction in layered Ni-rich cathodes for Li-ion batteries. *Nat. Mater.* **20**, 84 (2021). doi:10.1038/s41563-020-0767-8
 16. K. Märker, P. J. Reeves, C. Xu, K. J. Griffith, C. P. Grey, Evolution of Structure and Lithium Dynamics in LiNi_{0.8}Mn_{0.1}Co_{0.1}O₂ (NMC811) Cathodes during Electrochemical Cycling. *Chem. Mater.* **31**, 2545 (2019). doi:10.1021/acs.chemmater.9b00140
 17. C. Xu, P. J. Reeves, Q. Jacquet, C. P. Grey, Phase Behavior during Electrochemical Cycling of Ni-Rich Cathode Materials for Li-Ion Batteries. *Adv. Energy Mater.* **11**, 2003404 (2021). doi:10.1002/aenm.202003404
 18. C. Tian, Y. Xu, D. Nordlund, F. Lin, J. Liu, Z. Sun, Y. Liu, M. Doeff, Charge Heterogeneity and Surface Chemistry in Polycrystalline Cathode Materials. *Joule* **2**, 464 (2018). doi:10.1016/j.joule.2017.12.008
 19. C. Cao, M. F. Toney, T.-K. Sham, R. Harder, P. R. Shearing, X. Xiao, J. Wang, Emerging X-ray imaging technologies for energy materials. *Mater. Today* **34**, 132 (2020). doi:10.1016/j.mattod.2019.08.011
 20. J. Lu, T. Wu, K. Amine, State-of-the-art characterization techniques for advanced lithium-ion batteries. *Nat. Energy* **2**, 17011 (2017). doi:10.1038/nenergy.2017.11
 21. I. Martens, L. G. A. Melo, D. P. Wilkinson, D. Bizzotto, A. P. Hitchcock, Characterization of X-ray Damage to Perfluorosulfonic Acid Using Correlative Microscopy. *J. Phys. Chem. C* **123**, 16023 (2019). doi:10.1021/acs.jpcc.9b03924
 22. A. J. Merryweather, C. Schnedermann, Q. Jacquet, C. P. Grey, A. Rao, Operando optical tracking of single-particle ion dynamics in batteries. *Nature* **594**, 522 (2021). doi:10.1038/s41586-021-03584-2
 23. J. Ortega-Arroyo, P. Kukura, Interferometric scattering microscopy (iSCAT): new frontiers in ultrafast and ultrasensitive optical microscopy. *Phys. Chem. Chem. Phys.* **14**, 15625 (2012). doi:10.1039/C2CP41013C
 24. M. Piliarik, V. Sandoghdar, Direct optical sensing of single unlabelled proteins and super-resolution imaging of their binding sites. *Nat. Commun.* **5**, 4495 (2014). doi:10.1038/ncomms5495
 25. G. M. Reza, W. T. Richard, K. Martin, S. Susann, M. Mahdi, K. Kiarash, S. Vahid, Point spread function in interferometric scattering microscopy (iSCAT). Part I: aberrations in defocusing and axial localization. *Opt. Express* **28**, 25969–25988 (2020). doi:10.1364/OE.401374
 26. C. A. Marianetti, G. Kotliar, G. Ceder, A first-order Mott transition in Li_xCoO₂. *Nat. Mater.* **3**, 627 (2004). doi:10.1038/nmat1178

27. M. Ménétrier, D. Carlier, M. Blangero, C. Delmas, On “Really” Stoichiometric LiCoO₂. *Electrochem. Solid State Lett.* **11**, A179 (2008). doi:10.1149/1.2968953
28. M. Ménétrier, I. Saadoune, S. Levasseur, C. Delmas, The insulator-metal transition upon lithium deintercalation from LiCoO₂: electronic properties and ⁷Li NMR study. *J. Mater. Chem.* **9**, 1135 (1999). doi:10.1039/A900016J
29. W. Weppner, R. A. Huggins, Determination of the Kinetic Parameters of Mixed-Conducting Electrodes and Application to the System Li₃Sb. *J. Electrochem. Soc.* **124**, 1569 (1977). doi:10.1149/1.2133112
30. A. Verma, K. Smith, S. Santhanagopalan, D. Abraham, K. P. Yao, P. P. Mukherjee, Galvanostatic Intermittent Titration and Performance Based Analysis of LiNi_{0.5}Co_{0.2}Mn_{0.3}O₂ Cathode. *J. Electrochem. Soc.* **164**, A3380 (2017). doi:10.1149/2.1701713jes
31. K. Kang, Y. S. Meng, J. Bréger, C. P. Grey, G. Ceder, Electrodes with high power and high capacity for rechargeable lithium batteries. *Science* **311**, 977 (2006). doi:10.1126/science.1122152
32. M. D. Radin, S. Hy, M. Sina, C. Fang, H. Liu, J. Vinckeviciute, M. Zhang, M. S. Whittingham, Y. S. Meng, A. Van der Ven, Narrowing the Gap between Theoretical and Practical Capacities in Li-Ion Layered Oxide Cathode Materials. *Adv. Energy Mater.* **7**, 1602888 (2017). doi:10.1002/aenm.201602888
33. G. Dominika, C. Matthew, R. Carl, C. Christopher, K. Emma, Microstructural design of printed graphite electrodes for lithium-ion batteries. *Materials & Design* **205**, 109720 (2021). doi:10.1016/j.matdes.2021.109720
34. J. Asenbauer, T. Eisenmann, M. Kuenzel, A. Kazzazi, Z. Chen, D. Bresser, The success story of graphite as a lithium-ion anode material – fundamentals, remaining challenges, and recent developments including silicon (oxide) composites. *Sustainable Energy & Fuels* **4**, 5387 (2020). doi:10.1039/d0se00175a
35. F. Xin, H. Zhou, Y. Zong, M. Zuba, Y. Chen, N. A. Chernova, J. Bai, B. Pei, A. Goel, J. Rana, F. Wang, K. An, L. F. J. Piper, G. Zhou, M. S. Whittingham, What is the Role of Nb in Nickel-Rich Layered Oxide Cathodes for Lithium-Ion Batteries. *ACS Energy Letters* **1377** (2021). doi:10.1021/acseenergylett.1c00190

Acknowledgments: The authors are grateful to Umicore for providing the NMC material used in this work and to Dr Jérémie Auvergniot for helpful discussions.

Funding: This work was supported by the Faraday Institution Degradation Project [grant numbers FIRG001 and FIRG024]. A.J.M. acknowledges support from the EPSRC Cambridge NanoDTC, EP/L015978/1. C.S. acknowledges financial support by the Royal Commission of the Exhibition of 1851. A.R. acknowledge financial support from the EPSRC and the Winton Program for the Physics of Sustainability. This project has received funding from the European Research Council (ERC) under the European Union’s Horizon 2020 research and innovation programme (grant agreement no. 758826).

Author contributions: C.P.G, A.R. and C.S. conceived the idea of this work. C.X., A.J.M., Z.L. and C.S. performed the operando optical microscopy experiments. C.X. analysed the optical microscopy data with support from A.J.M., Z.L. and C.S. C.X. performed electrochemical

characterisations and SEM and analysed the data. Z.L. performed PXRD and C.X. performed Rietveld Refinement. S.S.P. developed the finite-element model under guidance of N.A.F and V.D and discussions with D.S.H. All authors discussed the results and contributed to the manuscript writing.

Competing interests: Authors declare that they have no competing interests.

Data and materials availability: All data are available in the main text or the supplementary materials.